



Title	Sub-nanometric High-Entropy Alloy Cluster: Hydrogen Spillover Driven Synthesis on CeO ₂ and Structural Reversibility
Author(s)	Hashimoto, Naoki; Mori, Kohsuke; Matsuzaki, Shuichiro et al.
Citation	JACS Au. 2023, 3(8), p. 2131-2143
Version Type	VoR
URL	https://hdl.handle.net/11094/92486
rights	This article is licensed under a Creative Commons Attribution-NonCommercial-NoDerivatives 4.0 International License.
Note	

The University of Osaka Institutional Knowledge Archive : OUKA

<https://ir.library.osaka-u.ac.jp/>

The University of Osaka

Sub-nanometric High-Entropy Alloy Cluster: Hydrogen Spillover Driven Synthesis on CeO₂ and Structural Reversibility

Naoki Hashimoto, Kohsuke Mori,* Shuichiro Matsuzaki, Kazuki Iwama, Ryota Kitaura, Naoto Kamiuchi, Hideto Yoshida, and Hiromi Yamashita



Cite This: *JACS Au* 2023, 3, 2131–2143



Read Online

ACCESS |

Metrics & More

Article Recommendations

Supporting Information

ABSTRACT: High-entropy alloy (HEA) nanoparticles (NPs) have attracted significant attention as promising catalysts owing to the various unique synergistic effects originating from the nanometer-scale, near-equimolar mixing of five or more components to produce single-phase solid solutions. However, the study of sub-nanometer HEA clusters having sizes of less than 1 nm remains incomplete despite the possibility of novel functions related to borderline molecular states with discrete quantum energy levels. The present work demonstrates the synthesis of CeO₂ nanorods (CeO₂-NRs) on which sub-nanometer CoNiCuZnPd HEA clusters were formed with the aid of a pronounced hydrogen spillover effect on readily reducible CeO₂ (110) facets. The CoNiCuZnPd HEA sub-nanoclusters exhibited higher activity during the reduction of NO by H₂ even at low temperatures compared with the corresponding monometallic catalysts. These clusters also showed a unique structural reversibility in response to repeated exposure to oxidative/reductive conditions, based on the sacrificial oxidation of the non-noble metals. Both experimental and theoretical analyses established that multielement mixing in quantum-sized regions endowed the HEA clusters with entirely novel catalytic properties.

KEYWORDS: high-entropy alloy, nanoparticles, sub-nanometer clusters, catalysis, CeO₂ nanorods, hydrogen spillover effect, NO reduction, structural reversibility, oxidative/reductive conditions, XANES spectra



INTRODUCTION

High-entropy alloys (HEAs) have attracted much attention in various fields with regard to applications as structural materials,¹ biomaterials,² supercapacitors,³ and catalysts.^{4,5} HEAs comprise mixtures of five or more metallic elements at near equiatomic ratios and form simple single solid-solution phases having lattice structures including face-centered cubic (fcc) and body-centered cubic (bcc).^{6,7} The high configurational entropy of these alloys stabilizes the solid-solution phase such that this phase appears rather than an intermetallic phase or phase segregation.^{8,9} The severe lattice distortion in these materials that results from differences in the atomic sizes of the constituent elements also causes low atomic diffusivity.¹⁰ The unique synergistic effects resulting from combining multiple elements provide high specific strength, ductility, corrosion resistance, and thermal stability, such that HEAs are unique and fascinating materials. In recent years, many researchers have reported that HEA nanoparticles (NPs) having sizes on the nanometer scale (that is, in the range of 1 to 100 nm) show promise with regard to catalytic applications. Various techniques for the synthesis of such NPs have been developed, including those based on the use of carbothermal shock,^{9,11,12} microwave radiation,¹³ ultrasonication,¹⁴ fast moving bed pyrolysis,¹⁵ and continuous flow reactors.^{16,17} Each of these processes is capable of fabricating thoroughly mixed HEA NPs

with homogenous size distributions. However, the synthesis of sub-nanometer HEA clusters (that is, clusters having sizes of less than 1 nm) remains challenging even though these materials may exhibit novel properties based on borderline molecular states with discrete quantum energy levels.

Hydrogen spillover is the term used to describe the migration of activated H atoms from noble metal NPs to the surfaces of the metal oxides on which they are supported. This phenomenon has applications in the fields of hydrogen storage materials,¹⁸ sensor fabrication,¹⁹ and heterogeneous catalysis.^{20,21} Hydrogen spillover is favored on reducible transition metal oxides such as TiO₂, CeO₂, and WO₃ because active H atoms are able to migrate over oxide surfaces as proton (H⁺)/electron (e⁻) pairs based on the reaction $M^{n+} + O^{2-} + H \rightarrow M^{(n-1)+} + OH^-$.²² Our group previously demonstrated that NPs made of binary solid-solution alloys having non-equilibrium compositions (specifically, Ru–Ni and Rh–Cu) can be synthesized by utilizing individual H atoms originating

Received: April 29, 2023

Revised: July 5, 2023

Accepted: July 6, 2023

Published: July 18, 2023



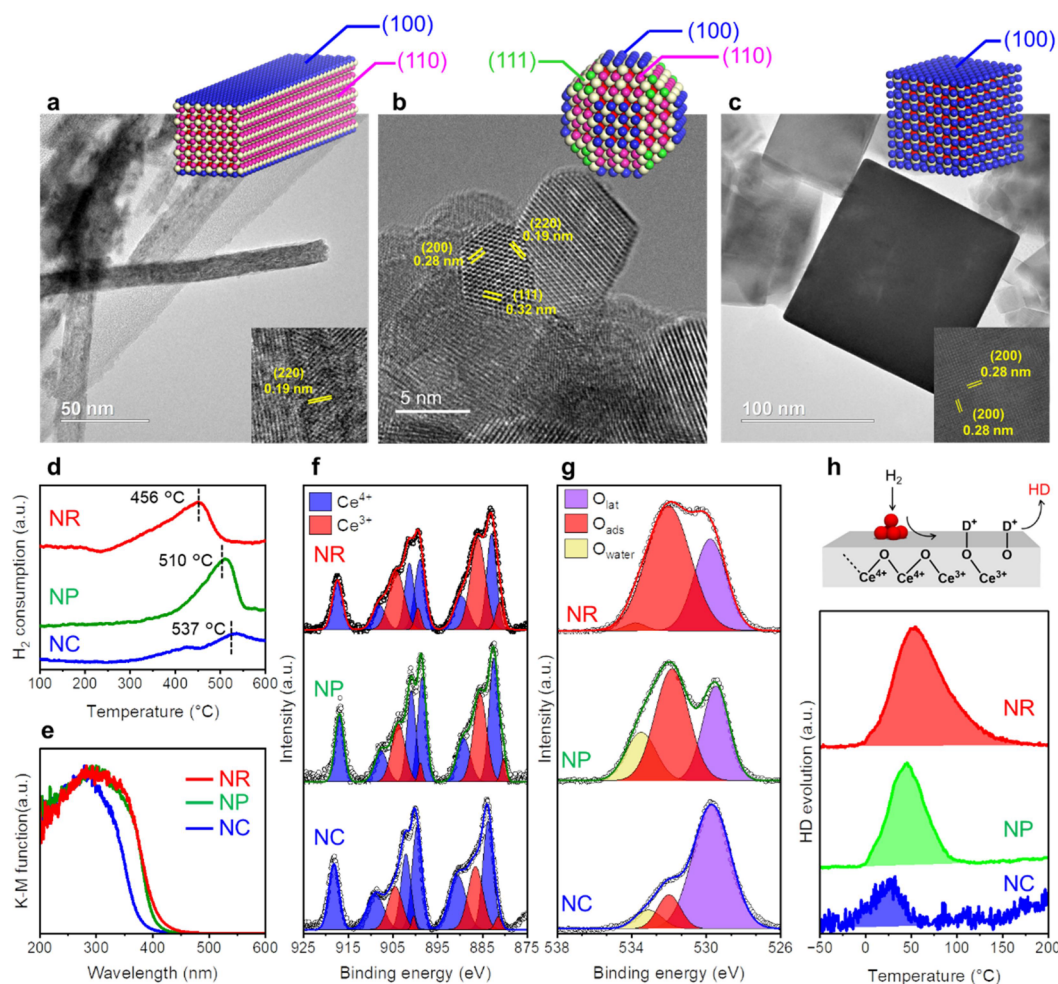


Figure 1. TEM images of (a) CeO₂-NRs, (b) CeO₂-NPs, and (c) CeO₂-NCs. Corresponding (d) H₂-TPR profiles and (e) UV-vis spectra of various CeO₂ supports. (f) Ce 3d and (g) O 1s XPS spectra were obtained from CeO₂-NRs, CeO₂-NPs, and CeO₂-NCs. (h) Mass spectra were obtained during HD evolution via hydrogen spillover using Pd/CeO₂ samples with different morphologies. Each mass spectrum was normalized relative to the S_{BET} for the material.

from hydrogen spillover as a strong reductant to promote the simultaneous rapid reduction of deposited metal cations at low temperatures.^{23–25} This prior work also involved the synthesis of CoNiCuRuPd HEA NPs with a mean diameter of 2 nm, in which there are large gaps between the reduction potentials of the constituent elements, using the pronounced hydrogen spillover effect of TiO₂.²⁶ The results of this research confirmed significantly improved catalytic activity and stability compared with monometallic catalysts during the hydrogenation of CO₂. These effects were attributed to the cocktail effect as well as to sluggish diffusion, the characteristic effects of HEA, originating from the synergistic effect obtained from this combination of elements.

Cerium oxide (CeO₂) is one of the most promising support materials and provides improved catalytic activity as a consequence of the strong synergistic effects that can be obtained by combining this oxide with supported NPs. These unique effects result from the reversible redox capacity of the Ce³⁺/Ce⁴⁺ pair, which in turn, is associated with the introduction of oxygen vacancies.^{27,28} Because exposed surface facets can significantly modify the properties of this material, including its catalytic activity, considerable effort has been devoted to elucidating the relationship between catalytic activity and the morphology of CeO₂.^{29–31} CeO₂ nanorods

(CeO₂-NRs) have been shown to preferentially expose four (110) facets and two (100) facets, while CeO₂ nanocubes (CeO₂-NCs) and CeO₂ nano-octahedra (CeO₂-NO) expose six (100) and eight (111) facets, respectively. Hu et al. demonstrated that Pd/CeO₂-NRs exhibit higher activity during CO oxidation than Pd/CeO₂-NCs and Pd/CeO₂-NO. Oxygen vacancies in Pd/CeO₂-NRs as well as the enhanced oxygen mobility in this material have also been found to play crucial roles in terms of promoting CO oxidation.³² Calculations based on density functional theory (DFT) have been used to assess the surface reactivity of CeO₂, and have indicated that the oxygen vacancy formation energy on each facet increases in the order of (110) < (100) < (111). These results suggest that surface (110) facets are more readily reduced and so are more likely to form oxygen vacancies.³³ Our group has previously demonstrated that Co-decorated CeO₂-NRs (CoCeO₂-NRs), which possess (110) facets, show superior catalytic activity and durability during carbon soot combustion compared with CoCeO₂ specimens having other morphologies, such as NC and nanopolyhedral.³⁴ The improved activity of CoCeO₂-NRs is primarily ascribed to the high oxygen release rate and significant redox activity of the (110) facets. Since CeO₂ is a reducible metal oxide support (owing to the low reduction potential between Ce³⁺ and Ce⁴⁺), hydrogen spillover on the

Table 1. Lattice Constants, Band Gaps, Surface Compositions, and Hydrogen Spillover Abilities of CeO₂ Supports

	lattice constant [Å]	band gap [eV]	Ce ³⁺ concentration [%]	O _{ads} concentration [%]	relative amount of HD yielded
CeO ₂ -NRs	5.435	2.82	40.6	64.5	4.4
CeO ₂ -NPs	5.428	2.93	36.9	59.9	2.6
CeO ₂ -NCs	5.416	3.08	35.8	15.2	1 (corrected)

CeO₂ surface is energetically favored.^{35,36} However, the effect of the CeO₂ morphology on hydrogen spillover has not yet been elucidated.

Herein, we describe a simple method for the fabrication of a HEA nanocatalyst that functions on the basis of the hydrogen spillover effect on a CeO₂ support. This work examined facet-dependent hydrogen spillover behavior and found that a CeO₂-NR support having exposed (110) planes provided enhanced hydrogen spillover compared with CeO₂-NCs and CeO₂-NPs specimens, thus producing sub-nanosized HEA clusters. The resulting CoNiCuZnPd HEA nanoclusters on a CeO₂-NR support exhibited high catalytic activity during the NO reduction reaction even at low temperatures. These results provide further evidence that HEA nanoclusters can show unique structural reversibility in response to repeated exposure to the oxidative/reductive atmospheres. The present study establishes a promising technique for the synthesis of ultrafine multimetal nanoclusters having novel properties as a consequence of the synergistic effects of multiple elements mixing in a quantum-sized region.

RESULTS AND DISCUSSION

Effects of Morphology on Hydrogen Spillover on CeO₂ Supports

CeO₂-NRs and CeO₂-NCs were prepared using a hydrothermal method while varying the reaction conditions. In contrast, the CeO₂-NPs were commercially available and so were simply purchased. TEM images of CeO₂ samples having different morphologies are shown in Figure 1a–c. The average thickness and length of the CeO₂-NRs were determined to be approximately 15 and 100 nm, respectively. Three types of lattice fringes, related to the (111), (200), and (220) planes of the material, were observed in the HR-TEM image acquired from this specimen (Figure S1). These analyses indicated that the CeO₂-NRs preferentially grew in the [110] direction and had exposed (110) facets. The CeO₂-NCs displayed a cubic structure with edge lengths in the range of 50–100 nm and were found to have only (100) exposed facets based on HR-TEM images (Figure S2).^{30,37} The CeO₂-NPs comprised edge-truncated particles, whose diameter is ca. 10 nm with low-index facets, such as (100), (110), and (111).³¹

The X-ray diffraction (XRD) diffraction patterns acquired from each of the CeO₂ samples contained distinct peaks related to a fluorite-like structure (Figure S3). The lattice constants calculated from the most intense (111) diffraction peaks increased in the order of CeO₂-NCs < CeO₂-NPs < CeO₂-NRs. These data suggest a higher degree of dispersion of Ce³⁺ ions in the CeO₂-NRs, presumably because of the larger atomic radius of Ce³⁺ compared with Ce⁴⁺ (Ce³⁺: 0.114 nm, Ce⁴⁺: 0.097 nm). The data obtained from the H₂ temperature-programmed reduction (H₂-TPR) experiments exhibited primary reduction peaks at 456, 510, and 537 °C for the CeO₂-NRs, CeO₂-NPs, and CeO₂-NCs, respectively (Figure 1d), indicating that the CeO₂-NRs promoted oxygen migration to the greatest extent and had the highest degree of surface

reducibility. A similar trend was observed in the case of the UV–vis diffuse reflectance spectra (Figure 1e). Specifically, the absorption edge position shifted to a longer wavelength in the order of CeO₂-NCs < CeO₂-NPs < CeO₂-NRs. The band structure were determined by the Tauc plot and the band gap for CeO₂-NRs (2.82 eV) became shorter than that of CeO₂-NPs (2.93 eV) and CeO₂-NCs (3.09 eV) (Figure S4). This effect is ascribed to the presence of surface oxygen vacancies.³⁸ The reducibility of each CeO₂ sample was also assessed by X-ray photoelectron spectroscopy (XPS) data, as shown in Figure 1f,g. The Ce 3d spectra could be deconvoluted into several peaks attributed to Ce³⁺ and Ce⁴⁺ species, and the results of quantitative analyses are summarized in Table 1. The fraction of Ce³⁺ in the material (Ce³⁺/(Ce³⁺ + Ce⁴⁺)) was found to increase in the order of CeO₂-NCs < CeO₂-NPs < CeO₂-NRs. The O 1s spectra could be fitted with three peaks, ascribed to lattice oxygen (O_{lat}), weakly surface adsorbed oxygen with a low coordination value (O_{ads}), and surface adsorbed water molecules (O_{water}). The O_{ads} was derived from active oxygen species adsorbed on exposed surface oxygen vacancies. The ratio of the O_{ads} amount relative to the total oxygen atoms (O_{ads}/(O_{ads} + O_{lat})) on the CeO₂-NRs was higher than that for the CeO₂-NPs and CeO₂-NCs, indicating a correlation with the proportion of Ce³⁺ in these materials.

The hydrogen spillover ability of each CeO₂ support was assessed by performing H/D exchange reactions. In these experiments, the Pd/CeO₂ was first exposed to a D₂ atmosphere at 300 °C to generate metallic Pd NPs on the CeO₂ and introduce O–D bonds on the CeO₂ surfaces. Subsequently, each sample was first cooled to –50 °C and then heated to 200 °C under H₂. The yield of HD from each trial was assessed by monitoring the signal obtained at *m/z* = 3 using mass spectroscopy. The associated surface reaction was 2H_{ad} + O_{lat} – D → HD (g) + O_{lat} – H, where H_{ad} is an adsorbed H atom, O_{lat} is lattice oxygen in the CeO₂, and HD (g) is gaseous HD generated via hydrogen spillover.³⁹ Note that, to exclude the effects of the surface area, all mass spectra were normalized by the corresponding specific surface area. The Pd/CeO₂-NRs produced the most intense HD peak in the temperature range of 0 to 150 °C (Figure 1h), exceeding those produced by the Pd/CeO₂-NPs and Pd/CeO₂-NCs by factors of 2.6 and 4.4, respectively.

Evidently, the CeO₂-NRs (which possessed exposed (110) facets) represented the most readily reducible CeO₂ support and so were the most likely to produce Ce³⁺ ions and oxygen vacancies. Additionally, more hydrogen atoms were consumed on the surface of the CeO₂-NRs during the H/D exchange reaction. These results suggest that the CeO₂-NR material was the most likely to promote hydrogen spillover because this phenomenon involved simultaneous proton–electron transfer associated with the reversible reduction and oxidation of the metal oxide (that is, Ce⁴⁺ + e[–] ↔ Ce³⁺).

Hydrogen Spillover-Assisted Synthesis and Characterization of HEA Catalysts

Three types of CoNiCuZnPd/CeO₂ specimens were synthesized, utilizing a conventional impregnation method. In this

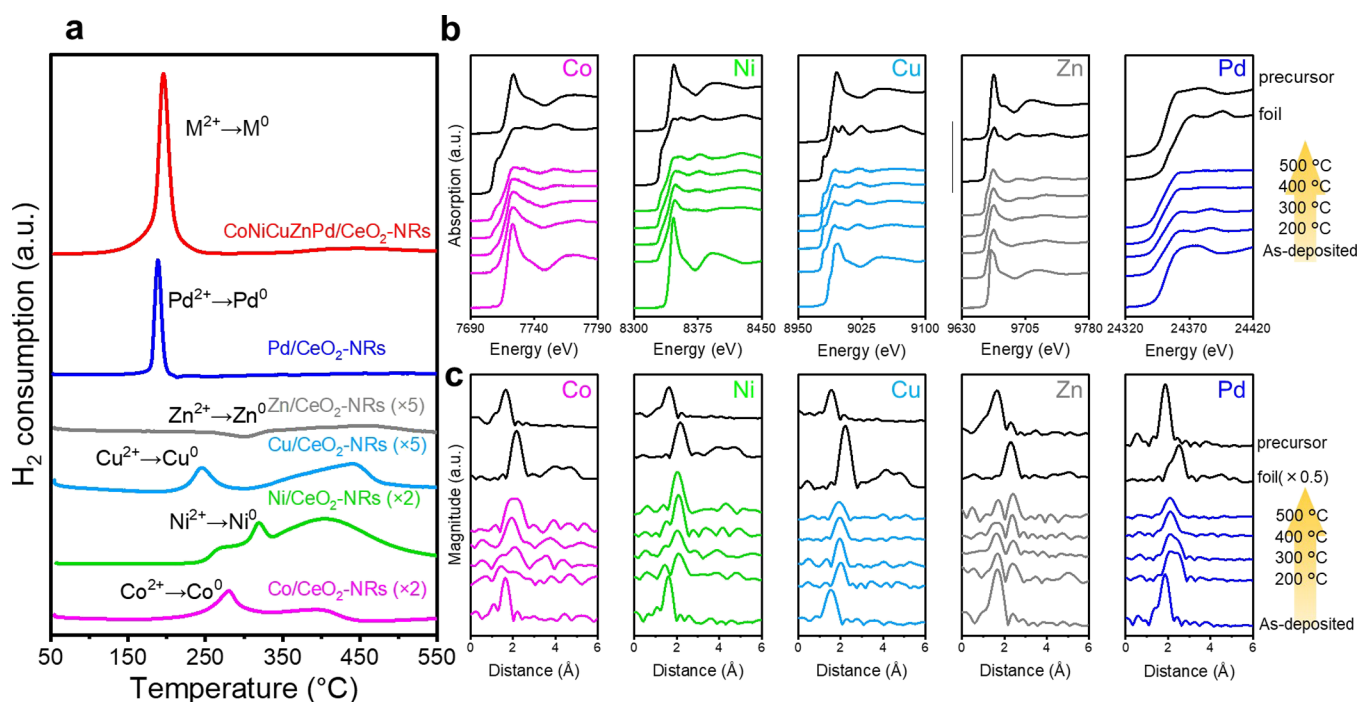


Figure 2. (a) H₂-TPR profiles of as-deposited monometallic and quinary component specimens. (b) *In situ* XANES and (c) FT-EXAFS spectra of CoNiCuZnPd/CeO₂-NRs acquired between room temperature and 500 °C under a flow of H₂.

process, all the metal precursors were deposited on each CeO₂ support, followed by reduction under a hydrogen atmosphere at 600 °C. This combination of elements was selected based on the moderately different reduction potentials for these metals ($E^0(\text{Co}^{2+}/\text{Co}^0) = -0.28$ V, $E^0(\text{Ni}^{2+}/\text{Ni}^0) = -0.26$ V, $E^0(\text{Cu}^{2+}/\text{Cu}^0) = +0.34$ V, $E^0(\text{Zn}^{2+}/\text{Zn}^0) = -0.76$ V, and $E^0(\text{Pd}^{2+}/\text{Pd}^0) = +0.99$ V, all vs a normal hydrogen electrode). Especially, the use of the transition metals such as Pd is crucial to initiate hydrogen spillover that enable the simultaneous reduction of precursors, as discussed later. The formation of a solid-solution phase from a multimetallic system requires a specific difference

in atomic size ($\delta < 6.6\%$ $\delta = \sqrt{\sum_{i=1}^n x_i \left(1 - \frac{r_i}{\bar{r}}\right)^2} \times 100$) and in configurational enthalpy ($-11.6 < \Delta H_{\text{mix}} < 3.2$ kJ/mol, $\Delta H_{\text{mix}} = 4 \sum_{j=1}^n \sum_{i=1}^n x_i x_j \Delta H_{ij}$) where x_i , r_i , \bar{r} , and ΔH_{mix} are the mole fraction of *i*th component, the atomic radius of the *i*th component, the average of atomic radius of the components, and the mixing enthalpy of the *i*th and *j*th component with the molar ratio of 1:1.⁴⁰ The present CoNiCuZnPd combination satisfied these criteria ($\delta = 3.8\%$, $\Delta H_{\text{mix}} = -8.2$ kJ/mol) and so the formation of an HEA was expected.

The reduction of supported metal cations was monitored by H₂-TPR analyses of as-deposited monometallic and quinary specimens prior to exposure to H₂. As shown in Figure 2a, the CeO₂-NRs in combination with single metal cations generated broad reduction peaks. The order of the reduction temperatures for these elements also corresponded to the order of their reduction potentials. Interestingly, the quinary CoNiCuZnPd/CeO₂-NR specimen produced a single sharp reduction peak at approximately 200 °C, which was almost equivalent to the temperature at which the monometallic Pd/CeO₂-NR specimen generated peaks. These data establish that all the metal cations were reduced simultaneously on the CeO₂-NR surface to form a quinary solid-solution alloy. The

hydrogen spillover phenomenon occurring at the Pd nuclei evidently accelerated the reduction of Co²⁺, Ni²⁺, Cu²⁺, and Zn²⁺ ions, despite the different redox potentials of these elements. A similar sharp reduction peak was also observed in the case of the CoNiCuZnPd/CeO₂-NPs, but the peak intensity is low, and the observed temperature increased to 260 °C (Figure S5A). Whereas the CoNiCuZnPd/CeO₂-NCs provided a relatively broad reduction peak. These results indicate that efficient hydrogen spillover took place on CeO₂-NRs compared with CeO₂-NPs and CeO₂-NCs, leading to a uniform simultaneous reduction of the deposited metal precursors. In the separate experiment, the H₂-TPR profiles of as-deposited quinary component specimens for small CeO₂-NCs with edge length in the range of 10–20 nm ($S_{\text{BET}} = 33.0$ m² g^{−1}) exhibited almost same reduction peaks with that of the larger one with edge length in the range of 50–100 nm ($S_{\text{BET}} = 15.9$ m² g^{−1}) (Figure S5B). This result suggests that the differences in H-spillover ability is mainly induced by the difference in exposed crystal facets and the effect of the size of CeO₂ support is negligible.

High-angle annular dark-field scanning transmission electron microscopy (HAADF-STEM) images and corresponding energy-dispersive X-ray (EDX) elemental maps of CoNiCuZnPd/CeO₂-NRs are provided in Figure S6. The presence of metallic NPs is difficult to distinguish in the case of the CoNiCuZnPd/CeO₂-NRs because of the poor Z-contrast between the CoNiCuZnPd alloy and the CeO₂ support. However, the EDX map acquired over a specific region clearly shows all elements with the molar ratio of Co:Ni:Cu:Zn:Pd = 20:19:16:10:35 (Figure S6h). This result meets the criteria of HEA (that is, near atomic ratio (5–35 at%)), suggesting the formation of small HEA clusters in the region. Moreover, aberration-corrected scanning electron microscope (Cs-corrected SEM) image evidenced the presence of sub-nanocluster having diameters of less than 1 nm (Figure S7). On the contrary, quinary NPs can be observed to some extent in the

HAADF-STEM images and corresponding EDX maps on the CeO₂-NP support, although these NPs are seen to be relatively large (about 10 nm) and the position of each element evidently varies slightly within each particle (Figure S8). The CoNiCuZnPd/CeO₂-NCs image does not clearly show the formation of well-defined quinary NPs. Instead, small CoNi NPs approximately 5 nm in size together with large aggregated CuZnPd NPs approximately 20 nm in size are seen in the EDX map (Figure S9). These results are consistent with the H₂-TPR data and suggest that the CeO₂-NRs and CeO₂-NPs (but not the CeO₂-NCs) are suitable supports for the simultaneous rapid reduction of metal precursors and the formation of multielement NPs assisted by the hydrogen spillover effect.

The reduction sequences were examined in more detail by acquiring *in situ* X-ray absorption fine structure (XAFS) data under a H₂/He atmosphere between room temperature and 500 °C. The Cu and Pd K-edge X-ray absorption near-edge structure (XANES) spectra of the CoNiCuZnPd/CeO₂-NRs specimen obtained at 200 °C can be seen to be similar to those of the corresponding metallic foil reference materials, suggesting complete reduction below 200 °C (Figure 2b). In the case of Co, Ni, and Zn, whose reduction potentials are relatively low compared with those for Cu and Pd, the white line intensities in the XANES spectra were decreased even at 200 °C, suggesting that the precursors were partially reduced from M²⁺ to M⁰. It is worth noting that the shape of the spectra is almost identical to those of the corresponding foils after heating at 500 °C. A similar trend was observed in the case of the CeO₂-NP support (Figure S10). In contrast, the shape of the Pd K-edge XANES spectrum obtained from the CoNiCuZnPd/CeO₂-NC sample was closer to that of the metallic Pd rather than Pd²⁺ even at 200 °C, while that for Co, Ni, Cu, and Zn did not begin to change until approximately 300 °C (Figure S11). Additionally, the interaction of the different elements was observed in the *in situ* XANES spectra. In Figure 2b, the XANES spectra for non-noble metals at 500 °C showed the different pre-edge characteristic, which is attributed to 1s → 3d electron transition, in comparison with the corresponding monometallic foils, suggesting the electronic structure changes by alloying (that is, ligand effect).⁴² Especially, the E₀ value (measured at the half-height of the edge jump) of Pd atoms in CoNiCuZnPd/CeO₂-NRs shifted by −1.1 eV in comparison to that of Pd foils, which originated from the charge transfer from the non-noble metals to Pd owing to the net difference in electronegativity. Moreover, the fluctuation above the white line was red-shifted. This shift suggested that changes in the lattice constant from one of the monometallic foils.⁴¹ These results also supported that all non-noble metals contributed to the formation of quinary alloy.

Fourier-transform extended XAFS (FT-EXAFS) analyses were also conducted to further assess the structural transformations occurring during the reduction sequence (Figure 2c). The as-deposited CeO₂-NR specimen produced sharp singlet peaks attributable to M–O bonds at approximately 1.9 Å in all K-edge regions. The peaks due to Cu–O and Pd–O bonds disappeared at 200 °C, while a new peak related to M–M bonds with lengths of 2.0 to 2.5 Å appeared. In the case of Co, Ni, and Zn, the intensities of the peaks associated with M–O bonds began to decrease at 200 °C. These data provide clear evidence for the enhanced reduction of the base metals as a consequence of hydrogen spillover occurring on the CeO₂-NRs. Interestingly, the peaks due to M–M bonds for all elements indicated different bond lengths from those in the

corresponding metallic foils after heating at 500 °C. As an example, the Pd K-edge FT-EXAFS spectrum showed evidence for a metallic bond length of approximately 2.1 Å, which is shorter than the standard value of 2.5 Å. This outcome suggests that the Pd atoms were surrounded by elements having smaller atomic radii, such as Co, Ni, Cu, and Zn, rather than by other Pd atoms. It is notable that the Pd K-edge FT-EXAFS spectrum acquired at 200 °C exhibited two peaks due to Pd–M (M = Co, Ni, Cu and Zn) and Pd–Pd bonds at 2.1 and 2.5 Å, respectively, and that the Pd–Pd bonds gradually disappeared with increasing temperature and were completely gone above 400 °C. This result indicates that Pd nuclei were generated during the early stage of the reduction process, following which the other precursors were reduced to form the quinary HEA. Similarly, in the case of the CeO₂-NPs support, the Co, Ni, and Zn (along with the Pd and Cu) produced metallic bonds even at 200 °C under a H₂ atmosphere, demonstrating the contribution of the hydrogen spillover effect (Figure S12). However, the split of metallic bonds and the remain of Pd–Pd bonds even at 500 °C in Cu and Pd K-edge spectra, respectively, indicate that the coordination of these atoms was not homogeneous within each particle. Thus, partially phase-segregated NPs were formed on the CeO₂-NPs support rather than a well-mixed solid-solution phase, as confirmed by the STEM observations and elemental mapping.

The FT-EXAFS spectra acquired from the CoNiCuZnPd/CeO₂-NCs were quite different from those obtained from the CoNiCuZnPd/CeO₂-NRs (Figure S13). In the case of the base metals, the M–O bonds remained unchanged at 200 °C, although the Pd was completely reduced. The Pd K-edge FT-EXAFS spectra demonstrated the presence of both Pd–M and Pd–Pd bonds at 200 °C, and the intensity of the signal related to Pd–Pd bonds decreased with increasing temperature. However, this signal was still observed even at 400 °C. Moreover, the lengths of the Co–M bonds (2.2 Å) and Ni–M bonds (2.1 Å) at 400 °C were the same as those in the corresponding foils. These results suggest that all the elements were not homogeneously mixed and that Co and Ni were not involved in the formation of the alloy phase, in good agreement with the HAADF-STEM images of the CoNiCuZnPd/CeO₂-NCs.

Further insights into the local coordination spheres in these materials were obtained by determining the coordination numbers (CNs) and interatomic distances based on curve-fitting analyses of the Pd K-edge FT-EXAFS spectra (Figures 3a and S14). The data for each of the CoNiCuZnPd/CeO₂ specimens show the presence of Pd–Pd bonds at approximately 2.7 Å together with neighboring Pd–M bonds (M = Co, Ni, Cu, and Zn) at 2.6 Å (Table S1). Note that, because of the similar ionic radii of these 3d elements, the different Pd–M bonds could not be distinguished from one another and so these bonds were treated as equivalent during fitting.^{4,12} The total CN values (CN_{Pd–Pd} + CN_{Pd–M}) were determined to be 5.6, 11.4, and 10.9 for the CeO₂-NRs, CeO₂-NPs, and CeO₂-NCs, respectively. Assuming that the present clusters each had a *fcc* cuboctahedral lattice structure, the diameter of the quinary CoNiCuZnPd alloy cluster having a CN of 5.6 can be estimated to be 0.79 nm, consisting of an average of 13 atoms, according to the relationship between the CN and the diameter of a Pd cluster.⁴³ In addition, the Pd–Pd interatomic distance in the CoNiCuZnPd/CeO₂-NRs (2.70 Å) was found to be much shorter than that in the Pd foil (2.74 Å). This shrinkage provides further evidence for the presence of sub-

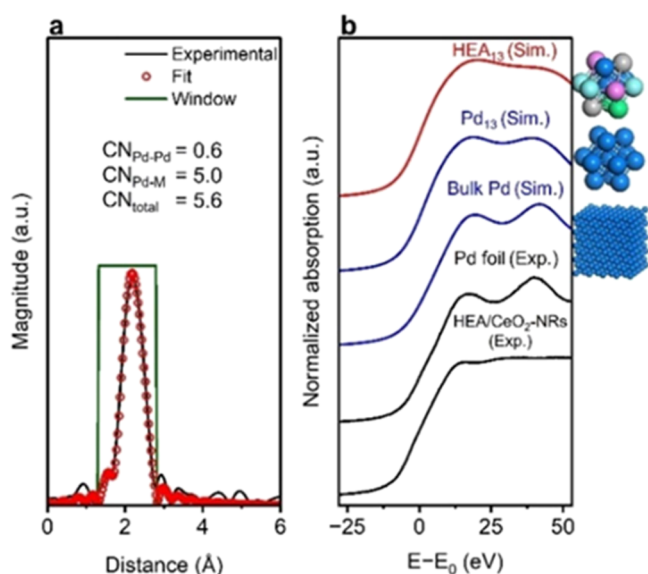


Figure 3. (a) Pd K-edge FT-EXAFS spectrum obtained from the CoNiCuZnPd/CeO₂-NRs and the fitting curve. (b) Experimental Pd K-edge XANES spectra of Pd foil and the CoNiCuZnPd/CeO₂-NRs (HEA/CeO₂-NRs), and the simulated XANES spectra of HEA₁₃ and Pd₁₃ clusters and of bulk Pd.

nanosized clusters.⁴⁴ Overall, such data suggest that CeO₂-NRs can serve as a promising platform for the synthesis of sub-nanometer HEA clusters based on the significant hydrogen spillover effect on this support.

Interestingly, the Pd K-edge XANES spectrum of the CoNiCuZnPd/CeO₂-NRs showed a unique featureless shape in the post-edge region without the two characteristic peaks at 24,390 and 24,415 eV attributed to electron transition from the 1s to 5p and 4f orbitals, respectively. These peaks are typically obtained from metallic Pd.⁴⁵ Hence, DFT-based simulations of the Pd K-edge XANES spectra were conducted to elucidate the structure of the quinary HEA supported on the CeO₂-NRs. The amplitudes of the oscillations in the post-edge region were also evaluated, employing several sets of models, and bulk Pd, bulk HEA, and Pd₁₃ cluster models produced fluctuating spectra (Figures 3b and S15). Conversely, the HEA₁₃(Co₂Ni₂Cu₃Zn₃Pd₃) cluster model reproduced a unique flat shape without obvious oscillations, further confirming that the CoNiCuZnPd alloy supported on the CeO₂-NRs comprised a well-mixed solid-solution phase with sub-nanometer clusters.

Based on the H₂-TPR and *in situ* XAFS results discussed above, a mechanism for the formation of HEA clusters on the CeO₂-NRs assisted by hydrogen spillover can be proposed (Figure 4). In this process, the supported Pd²⁺ cations are initially reduced to form Pd⁰ nuclei under a H₂ atmosphere. Following this, H₂ molecules are heterolytically dissociated at Pd/CeO₂ interfaces to form Pd–H and Ce–O–H species, accompanied by the reduction of neighboring Ce⁴⁺ ions to Ce³⁺ (step 1). Electron transfer from Ce³⁺ ions to adjacent Ce⁴⁺ ions promotes the simultaneous migration of H⁺ to O²⁻ anions attached to these contiguous Ce⁴⁺ ions (step 2). In this manner, H atoms and electrons rapidly diffuse over the CeO₂ surface, leading to the simultaneous reduction of other deposited precursor cations with large reduction potentials (step 3) to fabricate sub-nanometer HEA clusters (step 4). In the case of CeO₂-NP and CeO₂-NC supports, large quinary

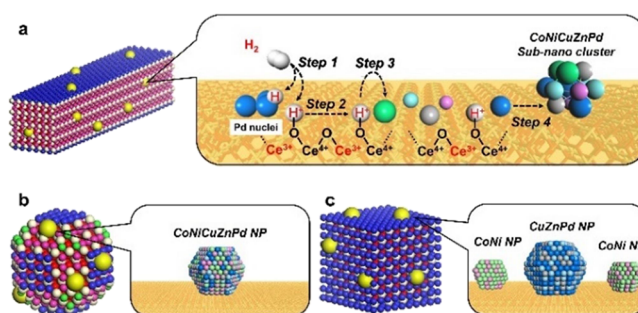


Figure 4. (a) Schematic illustration of elementary steps of the formation mechanism of HEA clusters on CeO₂-NRs. (b, c) Schematic illustrations supported NPs on CeO₂-NPs and CeO₂-NCs, respectively.

NPs and binary/ternary NPs were formed, respectively, due to the relatively low surface reducibilities and hydrogen spillover abilities of each CeO₂ support (Figure 4b,c). Our previous work revealed that the activation energy for the reduction of Mⁿ⁺ ion on TiO₂(101) by the spilled H (Langmuir–Hinshelwood mechanism) was substantially lower than those attained by a gaseous H₂ vapor (Eley–Rideal mechanisms).^{26,39} The energy barrier in Step 4 was determined by considering the formation energy of a five-nuclear cluster model containing five different elements from each reduced atom, which is lower than those in Steps 1–3. These preliminary analyses confirmed that the formation of HEA NPs is thermodynamically favored by the spilled H atoms by promoting the rapid and simultaneous reduction of the multiple metal precursors at low temperatures.

Catalytic Performance of CoNiCuZnPd/CeO₂ during NO Reduction

In the present work, catalytic nitric oxide (NO) reduction with H₂ was conducted as a benchmark reaction using the quinary alloy on the various CeO₂ supports. The effect of temperature on the catalytic activity between 50 and 200 °C is summarized in Figures 5 and S16.

The CoNiCuZnPd/CeO₂-NRs exhibited the highest activity at lower temperatures, giving an NO conversion of 100% at 100 °C. This temperature was considerably lower than those required when using NPs (150 °C) and NCs (200 °C) as supports. It should also be noted that the catalytic activity of

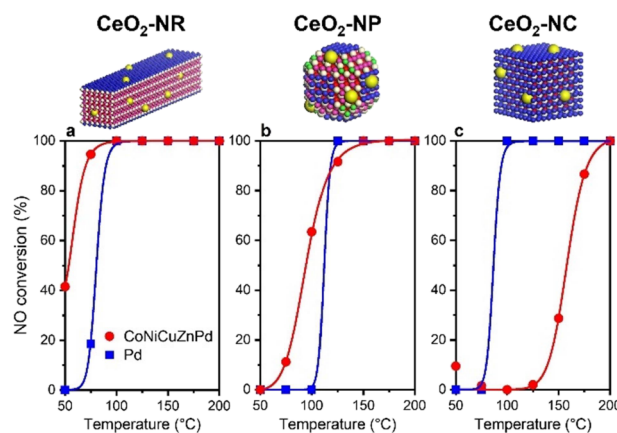


Figure 5. Catalytic NO reduction activity over quinary CoNiCuZnPd alloy and monometallic Pd catalysts supported on (a) CeO₂-NRs, (b) CeO₂-NPs, and (c) CeO₂-NCs.

the CoNiCuRuPd/CeO₂-NR sample was substantially higher than that of Pd/CeO₂-NRs prepared by the same method. Furthermore, other non-noble metal catalysts (that is, M/CeO₂-NRs where M = Co, Ni, Cu, or Zn) exhibited essentially zero NO reduction activity at 200 °C, as shown in Figure S17. Similarly, the CoNiCuZnPd/CeO₂-NPs provided improved activity in comparison with the corresponding monometallic Pd/CeO₂-NPs catalyst at low temperature, confirming the partial formation of a quinary HEA, albeit with relatively large cluster sizes on the nanometer scale. Conversely, the CoNiCuZnPd/CeO₂-NCs exhibited lower activity than the Pd/CeO₂-NCs, presumably because of the absence of HEA NPs. These results suggest that the formation of HEA improves the catalytic NO reduction activities in comparison to monometallic Pd catalysts (e.g., CoNiCuZnPd/CeO₂-NRs vs Pd/CeO₂-NRs and CoNiCuZnPd/CeO₂-NPs vs Pd/CeO₂-NPs) due to the synergistic effects of multiple elements (that is, the so-called cocktail effect). Additionally, the sub-nanometer HEA clusters formed on the CeO₂-NRs exhibited not only the cocktail effects but also the quantum size effects, as discussed below, and functioned better for NO reduction.

Another possible reason for the improved performance of the HEA sub-nanoclusters is the presence of under-coordinated surface atoms, which would be expected to drastically affect the capacity of the material to adsorb reactants.^{46,47} The adsorption characteristics of the monometallic and quinary alloy catalysts on the CeO₂-NRs were therefore assessed using temperature-programmed desorption (TPD) following NO adsorption in conjunction with Fourier-transform infrared spectroscopy (FT-IR) (Figure 6a,b). The

Pd/CeO₂-NRs sample generated the three peaks at around 1740, 1680, and 1590 cm⁻¹, attributed to linear-stretching vibrations of NO (ν_{NO}) adsorbed on-top, as twin type, and hollow sites respectively.⁴⁸ In addition, the intensities of the ν_{NO} peak attributed to the on-top sites obtained from the monometallic Pd/CeO₂-NRs specimens gradually decayed with increasing temperature, and almost NO molecules were desorbed from the Pd at 100 °C. In contrast, the CoNiCuZnPd/CeO₂-NRs continued to produce this peak even at 100 °C. These results suggest that the adsorption sites provided by the CoNiCuZnPd/CeO₂-NRs, strengthened the interaction of the material with NO molecules via electron enrichment, as also confirmed by the XANES spectra.

DFT calculations were also performed to provide support for these experimental results. The adsorption energy values (E_{ad}) for NO and H on *fcc* on-top, *fcc* hollow, and *hcp* hollow sites were evaluated in this manner. In preparation for these calculations, a CoNiCuZnPd HEA model slab was constructed by randomly populating each constituent atom in the *fcc* (111) facets of repeating slabs. A total of 25 different elemental distribution patterns were employed for the *fcc* on-top calculations together with 30 different patterns for the *fcc* hollow and *hcp* hollow models so as to investigate the effects of the HEA configuration (Tables S2–S4). The E_{ad} values for NO and H adsorbed at *fcc* on-top, *fcc* hollow, and *hcp* hollow sites on CoNiCuZnPd HEA slabs and the corresponding monometallic slabs are summarized in Figures 6c,d and S18.

For *fcc* on-top adsorption, each element was found to more strongly adsorb NO molecules in the case of the HEA slab rather than the corresponding monometallic slab. However, the H E_{ad} values were identical between the HEA and monometallic models. Similar trends were observed for *fcc* and *hcp* hollow sites. The NO E_{ad} on the hollow sites associated with the HEA slab was also higher than the average value for the monometallic models, while the H E_{ad} on these same sites was almost unchanged from the average value for the monometallic slabs. Furthermore, the adsorption energies were also calculated using the HEA cluster model containing 13 atoms to evaluate the size effects. As shown in Figure S19, all elements within the HEA cluster strongly adsorbed NO compared to the corresponding elements within the HEA slabs. Similarly, the adsorption energies of the H atom for non-noble metals within the HEA cluster slightly improved in comparison with those obtained within the HEA slab, while the adsorption energy of the H atom on Pd within the HEA cluster is comparable to that attained with the HEA slabs. These experimental and theoretical results demonstrate that the formation of HEA improved the NO adsorption more than the H adsorption. The strengthening of the interactions between NO molecules and the metal surface would be expected to weaken N–O bonds and thus promote the dissociation of these bonds. This effect is attributed to greater electron donation and back-donation based on d-5 σ and d-2 π^* interactions, respectively.⁴⁸ Thus, the NO reduction ability of the CoNiCuZnPd/CeO₂-NRs was improved.

Reversible Structural Change of HEA Sub-Nanoclusters

The stability of the present catalyst under oxidative/reductive conditions is a key factor affecting the application of this material to automotive emissions control. This stability was therefore assessed by monitoring changes in local structure using *in situ* XAFS. The experimental protocol and the resulting spectra are presented in Figures S20–S26. Figure 7a

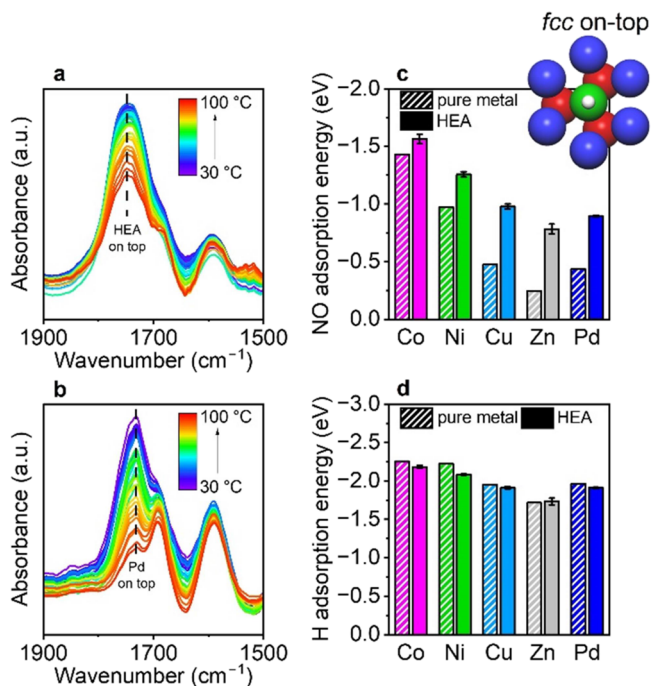


Figure 6. *In situ* FT-IR spectra were acquired during NO-TPD experiments for (a) CoNiCuZnPd/CeO₂-NRs and (b) Pd/CeO₂-NRs. The energies calculated for the adsorption of (c) NO and (d) H on *fcc* on-top sites for CoNiCuZnPd(111) and for monometallic slabs comprising Co(0001), Ni(111), Cu(111), Zn(0001), and Pd(111). Note that the E_{ad} values for CoNiCuZnPd(111) are the averages of those obtained from 25 HEA slab configurations. The error bars represent the corresponding standard deviations.

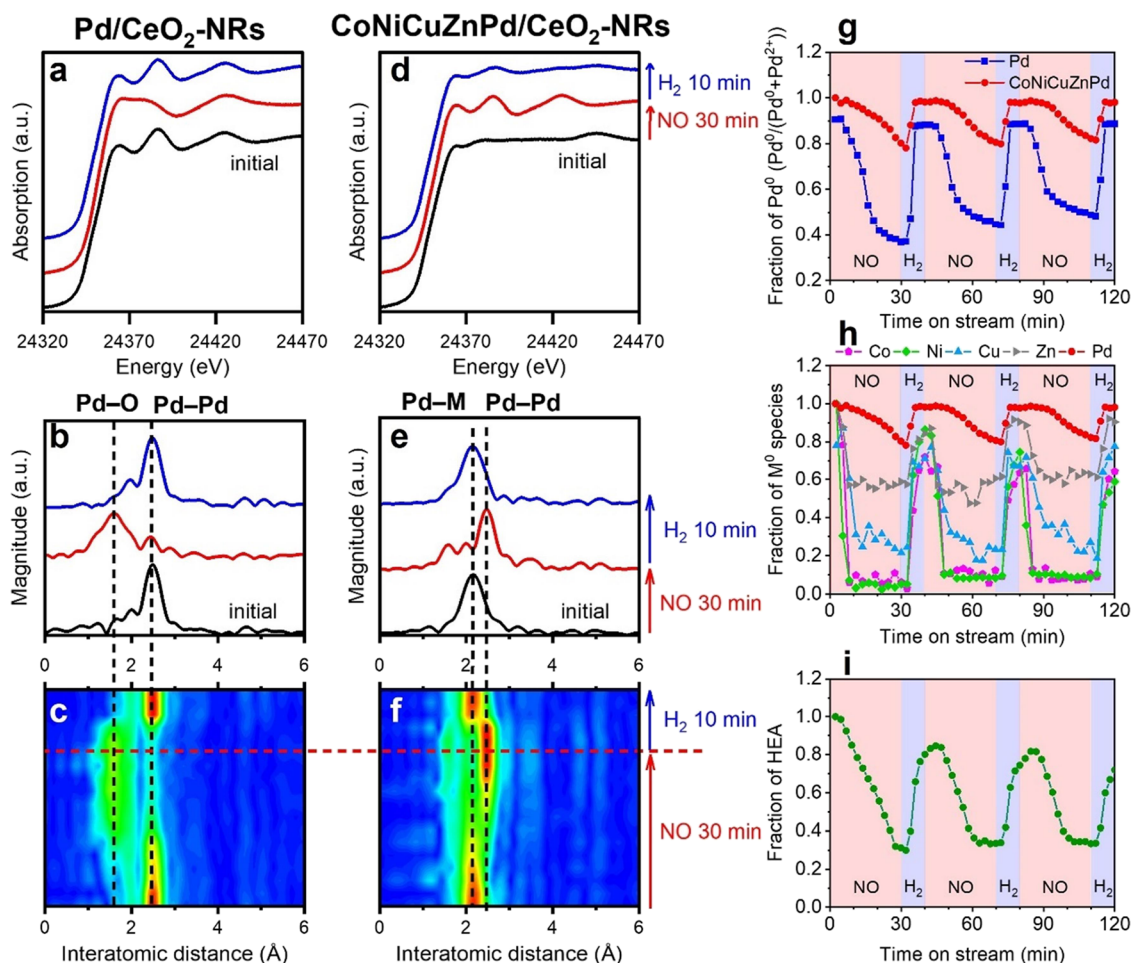


Figure 7. Pd K-edge *in situ* XANES spectra obtained from the (a) Pd/CeO₂-NRs and (d) CoNiCuZnPd/CeO₂-NRs under the flow of NO/H₂ at 400 °C. Pd K-edge *in situ* FT-EXAFS spectra obtained from (b, c) Pd/CeO₂-NRs and (e, f) CoNiCuZnPd/CeO₂-NRs under the flow of NO/H₂ at 400 °C. Fractions of (g) metallic Pd species in Pd/CeO₂-NRs and CoNiCuZnPd/CeO₂-NRs and of (h) M⁰ species and (i) HEA in CoNiCuZnPd/CeO₂ under the flow of NO/H₂, as determined by linear combination fitting (LCF) of XANES spectra.

shows the Pd K-edge XANES spectra obtained at 400 °C under either an oxidative (8000 ppm NO/He) or reductive (20,000 ppm H₂/He) atmosphere. The data initially acquired from the Pd/CeO₂-NRs indicate Pd in the metallic state but the edge position is shifted to a higher energy under NO, accompanied by a gradual change in the shape in the post-edge region. These variations are indicative of the oxidation of Pd. Following the introduction of H₂, the edge position returned to the initial lower energy value and two characteristic peaks related to metallic Pd appeared. These changes were also observed even after successive oxidation and reduction.

The FT-EXAFS spectra provided further evidence for the above scenario (Figure 7b,c). The intensity of the initial main peak due to Pd–Pd bonds at approximately 2.5 Å decreased under NO, accompanied by an increase in the peak related to Pd–O bonds at approximately 1.6 Å. Following the introduction of H₂, the latter peak disappeared and the Pd–Pd peak was recovered. These results are clear evidence for the reversible redox capabilities of Pd species on monometallic Pd/CeO₂ catalysts under oxidative/reductive conditions, as has been reported previously.⁴⁹

Interestingly, the CoNiCuZnPd/CeO₂-NR specimen exhibited different regeneration properties from those for monometallic Pd/CeO₂-NRs (Figure 7d–f). The initially flat XANES spectrum transitioned to a shape typical of

monometallic Pd upon the introduction of NO. In the case of the FT-EXAFS spectra, the peak attributed to short Pd–M bonds at approximately 2.1 Å disappeared and a peak related to long Pd–Pd bonds gradually appeared. These data clearly suggest that the oxidation of Pd species was suppressed even upon exposure to NO, with the other metals acting as sacrificial species to prevent this oxidation. After switching to a H₂ flow, the XANES spectrum regained the flat shape characteristic of the HEA. The FT-EXAFS spectrum also recovered the original HEA structure with decreasing and increasing intensity of peaks associated with long Pd–Pd bonds and short Pd–M bonds, respectively.

Linear combination fitting (LCF) of these Pd K-edge XANES spectra provided further information regarding the oxidation state of each metal during the redox sequence. As shown in Figure 7g, the Pd⁰ fraction (Pd⁰/(Pd⁰ + Pd²⁺)) in the Pd/CeO₂-NRs was initially 0.90 but subsequently decreased to 0.37 after the introduction of NO for 30 min, and then returned to its initial value under a reductive H₂ atmosphere. Conversely, the oxidation of Pd species in the CoNiCuZnPd/CeO₂-NRs was suppressed and a fraction of 0.78 was observed even after a 30 min exposure to NO. Moreover, the Pd in this material was almost entirely reduced to the metallic state upon the introduction of H₂. It should also be noted that the Pd species in the CoNiCuZnPd/CeO₂-NRs sample exhibited

almost complete reversibility of this process following successive oxidation and reduction.

The fraction of M^0 species among all the elements in the CoNiCuZnPd/CeO₂-NRs was evaluated based on applying the LCF technique to XANES spectra. As summarized in Figure 7h, each of the base metals was oxidized under NO but returned to the metallic form under H₂. It should be noted that Co and Ni were oxidized completely, while Cu and Zn were only partially oxidized during exposure to NO. Figure 7i show the HEA proportions determined by the LCF analyses of Pd K-edge XANES spectra of Pd foil and the original CoNiCuZnPd/CeO₂-NRs. Under NO, this proportion decreased from 1 to 0.31, but following the introduction of H₂, the HEA structure was recovered.

From these results, differences in the mechanisms responsible for the structural reversibility of the monometallic and quinary catalysts under oxidative/reductive conditions can be proposed (Figure 8). Monometallic Pd NPs on the CeO₂-

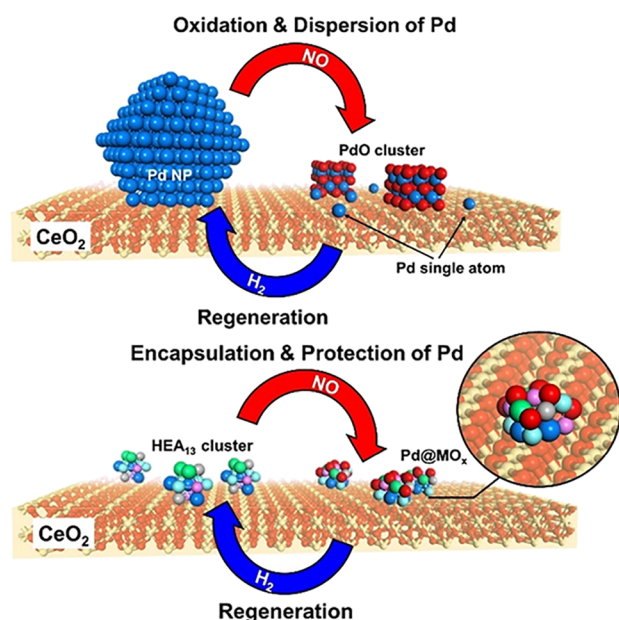


Figure 8. Proposed structural changes of monometallic Pd and quinary CoNiCuZnPd alloy supported on CeO₂-NRs upon exposure to NO/H₂.

NRs, which were determined to have diameters of approximately 2 nm based on curve fitting of FT-EXAFS data, were easily oxidized and dispersed on the CeO₂. These NPs were therefore transformed into PdO clusters and single atom Pd^{δ+} species under oxidative NO conditions, and subsequently transitioned back to NPs by reduction with H₂.^{50,51} In the case of the CoNiCuZnPd/CeO₂-NRs, the randomly distributed Pd atoms formed core nuclei encapsulated by non-noble metal oxide shells (that is, Pd@MO_x; M = Co, Ni, Cu, and Zn) via the sacrificial oxidation of the base metals, which are easily oxidized under NO. These oxide shells provided steric hindrance to interactions between the Pd atoms and NO molecules and also inhibited the diffusion of Pd atoms into the CeO₂. It is notable that the morphology of the 13-atom nanoclusters changed from spherical cuboctahedral to raft-like, and that this change limited the exposure of Pd atoms. These structures could be reversibly changed back to well-mixed HEA nanoclusters under a H₂ atmosphere via reduction of oxide

shell and atomic diffusion to transform from core-shell to random structure by the contribution of entropic effects. This proposed model based on Pd@MO_x clusters having raft-like morphologies can be confirmed based on a Pd₃@(Co₃Ni₂Cu₃Zn₂)O₆ model, as illustrated in Figure S27a. The simulated Pd K-edge XANES spectrum contained two characteristic peaks due to monometallic Pd⁰, in sharp contrast to the spectrum obtained for metallic HEA clusters (that is, the HEA₁₃ clusters). It should be noted that the XANES simulation of the partially oxidized cuboctahedral cluster showed a flat spectrum, not fluctuated one (Figure S27b). This result further confirms that sub-nanometric clusters undergo not only the sacrificial oxidation of non-noble metals but also the structural transformation from cuboctahedral into raft-like form in NO atmosphere.

CONCLUSIONS

HEA nanoclusters were synthesized with the aid of the strong hydrogen spillover effect on CeO₂ surfaces, and the effects of the CeO₂ morphology were evaluated by both experimental observations and theoretical calculations. CeO₂-NRs containing highly reducible (110) surfaces enabled the synthesis of sub-nanometer HEA clusters of an average owing to the simultaneous rapid reduction of precursors ions having different reduction potentials. Conversely, CeO₂-NPs produced aggregated quinary NPs exhibiting partial segregation, while binary and ternary NPs were formed on the CeO₂-NCs. The CoNiCuZnPd/CeO₂-NRs showed higher catalytic activity and stability during NO reduction with H₂ compared with monometallic Pd/CeO₂-NRs. This improved performance originated from a cocktail effect caused by the combination of multiple metals. *In situ* XAFS observations under consecutive NO and H₂ atmospheres demonstrated the unique structural change properties of the quinary CoNiCuZnPd/CeO₂-NRs. This study highlights the importance of precisely tuning the exposed crystal facets of catalyst supports and also offers advanced insights into an innovative catalyst/photo-catalyst architecture based on sub-nanometer HEA clusters, while providing an understanding of the manner in which configurational variations affect catalytic performance. Further extension, including the detailed optimization of the components as well as their ratio, is under investigation.

EXPERIMENTAL

Materials

Ce(NO₃)₃·6H₂O, Co(NO₃)₂·6H₂O, Ni(NO₃)₂·6H₂O, Cu(NO₃)₂·3H₂O, Zn(NO₃)₂·6H₂O, and NaOH were purchased from Nacal Tesque. Na₂PdCl₄ was purchased from Tokyo Chemical Industry Co., Ltd. CeO₂-NPs (JRC-CEO-2, BET surface area (S_{BET}) = 130.1 m²·g⁻¹) was supplied by the Catalysis Society of Japan. All the reagents were used as received without any purification.

Preparation of Morphology-Controlled CeO₂ Supports

Morphology-controlled CeO₂ was synthesized using conventional hydrothermal method reported previously.^{52,53} The CeO₂-NRs (S_{BET} = 104.8 m²·g⁻¹) were prepared by adding a NaOH solution (175 mL, 11.4 M) dropwise to an aqueous solution of Ce(NO₃)₃·6H₂O (25 mL, 0.4 M). The mixture was stirred at room temperature for 1 h and then heated at 90 °C for 24 h in a Teflon cylinder sealed in a stainless-steel autoclave to produce the CeO₂-NRs specimen. CeO₂-NCs (S_{BET} = 15.9 m²·g⁻¹) were synthesized using the same process but with a different NaOH concentration (6 M) and reaction temperature (180 °C).

Preparation of Supported HEA Catalysts

CoNiCuZnPd/CeO₂ catalysts were prepared via a simple impregnation method. In this process, CeO₂ (500 mg) was dispersed in distilled water (100 mL), after which each metal precursor solution (10 mM) was added to the suspension with the following molar ratio (Co:Ni:Cu:Zn:Pd = 1:1:1:1:1). The mixture was subsequently stirred for 1 h and then evaporated by heating at 60 °C under vacuum. Finally, the specimen was reduced under a flow of hydrogen gas at 600 °C without any calcination.

Characterization

Temperature-programmed reduction by hydrogen (H₂-TPR) analysis was conducted using a BELCAT II apparatus (MicrotracBEL Corp.). Each specimen (50 mg) was preheated at 120 °C for 60 min under Ar to remove adsorbed water. Subsequently, the material was heated from 50 to 550 °C at a rate of 5 °C/min under a continuous flow of a 5% H₂/Ar mixture to obtain the TPR data. Surface H–D exchange profiles were also collected with the same instrumentation. In preparation for these trials, each sample was pretreated by heating at 300 °C under D₂ to reduce as-deposited Pd²⁺ ions and introduce O–D groups onto the CeO₂ surface. The reduced specimen was then cooled to –50 °C with liquid N₂ after which it was heated to 200 °C under a flow of a 5% H₂/Ar mixture. Field-emission transmission electron microscopy (FE-TEM) images were recorded with an instrument equipped with an EDX detector (Kevex), operating at an acceleration voltage of 200 kV. High-angle annular dark-field scanning transmission electron microscopy (HAADF-STEM) images were obtained using an instrument (Tecnai; Thermo Fisher Scientific) also equipped with an EDX detector (ARM200F; JEOL). Aberration-corrected scanning electron microscopy (Cs-corrected SEM) images were obtained with the HF 5000 (Hitachi High-Tech Corp.), operating at an acceleration voltage of 200 kV. UV–Vis diffuse reflectance spectra were obtained with a Shimadzu UV-2450 spectrophotometer, employing a Kubelka–Munk function and using BaSO₄ as a reference. XRD patterns were acquired using a Rigaku Ultima IV diffractometer with Cu K_α radiation (λ = 1.5406 Å). Brunauer–Emmett–Teller (BET) surface areas were calculated based on data obtained at –196 °C using a BELSORP Max apparatus (MicrotracBEL Corp.). All samples were degassed under vacuum at 130 °C for 3 h to remove adsorbed molecules as a pretreatment. XPS was performed with a Shimadzu ESCA-3400 system equipped with a Mg anode source ($h\nu$ = 1253.6 eV). The binding energy was calibrated using the C 1s core level at 284.5 eV, based on carbon present as a contaminant. XAFS spectra were obtained at the BL01B1 beamline station at the SPRING-8 facility, JASRI, Harima, Japan (proposal numbers 2022A1076 and 2021B1096), using a Si(111) monochromator. In preparation for these analyses, each sample was formed into a pellet and held in a batch-type *in situ* XAFS cell. During reduction sequence trials, the sample was reduced under a 45 mL/min flow of a 33% H₂/He mixture while heating at a rate of 10 °C/min to a constant temperature. The 3d elements (that is, Co, Ni, Cu, and Zn) were measured fluorescence mode, while 4d element (that is, Pd) was measured by transmission mode, respectively. The redox characteristics of the various materials under reaction conditions were assessed by first reducing each specimen under the same H₂/He flow by heating to 600 °C at 20 °C/min followed by a hold at that temperature for 2 h. This was followed by exposing the material in the *in situ* cell to a 50 mL/min flow of a mixture comprising 8000 ppm NO in He followed by a mixture comprising 20,000 ppm H₂ in He at a total flow of 50 mL/min while heating the cell at 400 °C. In the case of redox capacity test, all XAFS measurement were performed by transmission mode due to the requirement of quick responsibility. The XAFS data were processed using the Athena and Artemis programs included in the Demeter software package. NO-temperature-programmed desorption (TPD) data were acquired in conjunction with *in situ* FT-IR spectroscopy using a JASCO FT/IR-6600 instrument. In these trials, approximately 30 mg of samples were pressed into pellets that were then mounted in a specially designed quartz *in situ* IR cell (Makuhari Rikagaku Garasu). Each specimen was subsequently reduced by heating at 600 °C for 2 h under a flow of 20

mL/min H₂. Following this, each specimen was cooled to room temperature, after which the gas flow was switched to a mixture of 8000 ppm NO in He such that NO was adsorbed on the catalyst surface. After this step, any residual gaseous NO was purged with a flow of pure He. The NO-TPD profiles were obtained by heating the material from 30 to 100 °C at 2 °C/min under a He flow.

DFT Calculations

Adsorption energy values were calculated using DFT, employing the DMol³ program^{54,55} in the Material Studio 17.2 software package. The generalized gradient approximation exchange correlation functional proposed by Perdew, Burke, and Ernzerhof⁵⁶ combined with double numerical plus polarization was employed for geometry optimization. Two-layer slabs, each comprising 4 × 4 surface unit cells, were modeled in conjunction with a 20 Å vacuum gap along the z-axis to avoid interactions between the slabs. E_{ad} was calculated as $E_{\text{adsorbate/slab}} - (E_{\text{adsorbate}} + E_{\text{slab}})$, where $E_{\text{adsorbate/slab}}$, $E_{\text{adsorbate}}$, and E_{slab} are the total energy of the slab and adsorbate, the energy of the free adsorbate, and the energy of the bare slab, respectively.

Simulated XANES spectra were generated based on DFT calculations, employing the CASTEP package.^{57,58} Bulk Pd and HEA were modeled using 4 × 4 × 4 unit cells with a lattice length greater than 10 Å to avoid interactions between excited atoms, which were introduced core-hole.⁵⁹ The HEA bulk and HEA cluster model consisted of Co₁₃Ni₁₃Cu₁₂Zn₁₃Pd₁₃ and Co₇Ni₇Cu₃Zn₃Pd₃ having random configurations, respectively. Each of these cluster models having cuboctahedral morphologies together with *fcc* lattice structure was set in a vacuum unit cell with side lengths of 15 Å. All the models underwent geometric optimization, after which XANES spectra were simulated. An instrumental broadening factor was applied to adjust the oscillation amplitude of simulated spectra acquired from the Pd bulk model so as to match that of experimental spectra obtained from Pd foil.

Catalytic Activity Measurement

Catalytic activities were evaluated using a fixed-bed reactor system. In each trial, a 50 mg quantity of as-deposited catalyst was transferred into a quartz cell with an internal diameter of 4 mm held between two portions of quartz wool. Each specimen was pre-reduced by heating to 600 °C at a rate of 5 °C/min under a 20 mL/min flow of H₂ and holding at that temperature for 2 h followed by cooling to room temperature. Catalytic activity tests were then conducted under a 50 mL/min flow of a NO/H₂/He mixture containing 8000 ppm NO and 20,000 ppm H₂. The reaction products were analyzed with an online gas chromatograph (Shimadzu GC-2014 with a SHINWA SHIN-CARBON-ST column and a thermal conductivity detector).

ASSOCIATED CONTENT

Supporting Information

The Supporting Information is available free of charge at <https://pubs.acs.org/doi/10.1021/jacsau.3c00210>.

HR-TEM; XRD; Tauc plot; H₂-TPR; Cs-corrected SEM; HAADF-STEM; XANES spectra; FT-EXAFS spectra; XANES simulation; catalytic activity; DFT calculation; curve-fitting results at Pd K-edge for CoNiCuZnPd/CeO₂; list of employed 25 configuration patterns for the calculation of the adsorption energies; and list of employed 30 configuration patterns for the calculation of the adsorption energies (PDF)

AUTHOR INFORMATION

Corresponding Author

Kohsuke Mori – Division of Materials and Manufacturing Science, Graduate School of Engineering, Osaka University, Suita, Osaka 565-0871, Japan; Innovative Catalysis Science Division, Institute for Open and Transdisciplinary Research Initiatives (ICS-OTRI), Osaka University, Suita, Osaka 565-

0871, Japan; orcid.org/0000-0003-3915-4528;
Phone: +81-6-6879-7460; Email: mori@mat.eng.osaka-u.ac.jp; Fax: +81-6-6105-5029

Authors

Naoki Hashimoto – Division of Materials and Manufacturing Science, Graduate School of Engineering, Osaka University, Suita, Osaka 565-0871, Japan

Shuichiro Matsuzaki – Division of Materials and Manufacturing Science, Graduate School of Engineering, Osaka University, Suita, Osaka 565-0871, Japan

Kazuki Iwama – Division of Materials and Manufacturing Science, Graduate School of Engineering, Osaka University, Suita, Osaka 565-0871, Japan

Ryota Kitaura – Division of Materials and Manufacturing Science, Graduate School of Engineering, Osaka University, Suita, Osaka 565-0871, Japan

Naoto Kamiuchi – The Institute of Scientific and Industrial Research, Osaka University, Osaka 567-0047, Japan; orcid.org/0000-0002-4145-5226

Hideto Yoshida – The Institute of Scientific and Industrial Research, Osaka University, Osaka 567-0047, Japan

Hiromi Yamashita – Division of Materials and Manufacturing Science, Graduate School of Engineering, Osaka University, Suita, Osaka 565-0871, Japan; Innovative Catalysis Science Division, Institute for Open and Transdisciplinary Research Initiatives (ICS-OTRI), Osaka University, Suita, Osaka 565-0871, Japan

Complete contact information is available at:
<https://pubs.acs.org/10.1021/jacsau.3c00210>

Author Contributions

N.H. performed the catalyst preparation, calculation, and characterization, and wrote the manuscript. K.M. supervised the project. S.M., K.I., and R.K. helped with the catalyst preparation and characterization. N.K. and H.Y. performed the HAADF-STEM and EDX measurements. H.Y. helped to supervise the project. The manuscript was written through discussions with all authors. All authors have given approval to the final version of the manuscript. CRediT: **Naoki Hashimoto** investigation, writing-original draft; **Kohsuke Mori** investigation, supervision, writing-review & editing; **Shuichiro Matsuzaki** investigation; **Kazuki Iwama** investigation; **Ryota Kitaura** investigation; **Naoto Kamiuchi** investigation; **Hideto Yoshida** investigation; **Hiromi Yamashita** supervision.

Notes

The authors declare no competing financial interest.

ACKNOWLEDGMENTS

The present work was supported by the Kakenhi Grant-in-Aid for Transformative Research Areas(B) (No. 21B206). N.H. thanks JSPS for a Research Fellowship for Young Scientists (No. 22J20599). We acknowledge Hitachi High-Technologies Corporation for their assistance with the Cs-corrected SEM measurements (HF 5000). A part of TEM experiment was carried out by using a facility in the Research Center for Ultra-High Voltage Electron Microscopy, Osaka University. The synchrotron radiation experiments for XAFS measurements were performed at the BL01B1 beamline in SPring-8 with the approval from JASRI (2022A1076 and 2021B1096).

REFERENCES

- (1) Lim, K. R.; Lee, K. S.; Lee, J. S.; Kim, J. Y.; Chang, H. J.; Na, Y. S. Dual-phase high-entropy alloys for high-temperature structural applications. *J. Alloys Compd.* **2017**, 728, 1235–1238.
- (2) Hori, T.; Nagase, T.; Todai, M.; Matsugaki, A.; Nakano, T. Development of non-equiatomic Ti-Nb-Ta-Zr-Mo high-entropy alloys for metallic biomaterials. *Scr. Mater.* **2019**, 172, 83–87.
- (3) Xu, X.; Du, Y. K.; Wang, C. H.; Guo, Y.; Zou, J. W.; Zhou, K.; Zeng, Z.; Liu, Y. Y.; Li, L. Q. High-entropy alloy nanoparticles on aligned electrospun carbon nanofibers for supercapacitors. *J. Alloys Compd.* **2020**, 822, No. 153642.
- (4) Feng, G.; Ning, F.; Song, J.; Shang, H.; Zhang, K.; Ding, Z.; Gao, P.; Chu, W.; Xia, D. Sub - 2 nm Ultrasmall High-Entropy Alloy Nanoparticles for Extremely Superior Electrocatalytic Hydrogen Evolution. *J. Am. Chem. Soc.* **2021**, 143, 17117–17127.
- (5) Wu, D.; Kusada, K.; Yamamoto, T.; Toriyama, T.; Matsumura, S.; Kawaguchi, S.; Kubota, Y.; Kitagawa, H. Platinum-Group-Metal High-Entropy-Alloy Nanoparticles. *J. Am. Chem. Soc.* **2020**, 142, 13833–13838.
- (6) Cantor, B.; Chang, I. T. H.; Knight, P.; Vincent, A. J. B. Microstructural development in equiatomic multicomponent alloys. *Mater. Sci. Eng., A* **2004**, 375–377, 213–218.
- (7) Zhe, J. W.; Chen, S. K.; Lin, S. J.; Gan, J. Y.; Chin, T. S.; Shun, T. T.; Tsau, C. H.; Chang, S. Y. Nanostructured High-Entropy Alloys with Multiple Principal Elements: Novel Alloy Design Concepts and Outcomes. *Adv. Eng. Mater.* **2004**, 6, 299–303.
- (8) Yao, Y.; Huang, Z.; Hughes, L. A.; Gao, J.; Li, T.; Morris, D.; Zeltmann, S. E.; Savitzky, B. H.; Ophus, C.; Finck, Y. Z.; Dong, Q.; Jiao, M.; Mao, Y.; Chi, M.; Zhang, P.; Li, J.; Minor, A. M.; Shahbazian-Yassar, R.; Hu, L. Extreme mixing in nanoscale transition metal alloys. *Matter* **2021**, 4, 2340–2353.
- (9) Xie, P.; Yao, Y.; Huang, Z.; Liu, Z.; Zhang, J.; Li, T.; Wang, G.; Shahbazian-Yassar, R.; Hu, L.; Wang, C. Highly efficient decomposition of ammonia using high-entropy alloy catalysts. *Nat. Commun.* **2019**, 10, 4011.
- (10) Joo, S. H.; Bae, J. W.; Park, W. Y.; Shimada, Y.; Wada, T.; Kim, H. S.; Takeuchi, A.; Konno, T. J.; Kato, H.; Okulov, I. V. Beating Thermal Coarsening in Nanoporous Materials via High-Entropy Design. *Adv. Mater.* **2019**, 32, No. 1906160.
- (11) Yao, Y. G.; Huang, Z. N.; Xie, P. F.; Lacey, S. D.; Jacob, R. J.; Xie, H.; Chen, F. J.; Nie, A. M.; Pu, T. C.; Rehwoldt, M.; Yu, D. W.; Zachariah, M. R.; Wang, C.; Shahbazian-Yassar, R.; Li, J.; Hu, L. B. Carbothermal shock synthesis of high-entropy-alloy nanoparticles. *Science* **2018**, 359, 1489–1494.
- (12) Yao, Y.; Liu, Z.; Xie, P.; Huang, Z.; Li, T.; Morris, D.; Finck, Z.; Zhou, J.; Jiao, M.; Gao, J.; Mao, Y.; Miao, J.; Zhang, P.; Shahbazian-Yassar, R.; Wang, C.; Wang, G.; Hu, L. Computationally aided, entropy-driven synthesis of highly efficient and durable multi-elemental alloy catalysts. *Sci. Adv.* **2020**, 6, No. eaaz0510.
- (13) Qiao, H.; Saray, M. T.; Wang, X.; Xu, S.; Chen, G.; Huang, Z.; Chen, C.; Zhong, G.; Dong, Q.; Hong, M.; Xie, H.; Shahbazian-Yassar, R.; Hu, L. Scalable Synthesis of High Entropy Alloy Nanoparticles by Microwave Heating. *ACS Nano* **2021**, 15, 14928–14937.
- (14) Liu, M.; Zhang, Z.; Okejiri, F.; Yang, S.-Z.; Zhou, S.; Dai, S. Entropy-Maximized Synthesis of Multimetallic Nanoparticle Catalysts via a Ultrasonication-Assisted Wet Chemistry Method under Ambient Conditions. *Adv. Mater. Interfaces* **2019**, 6, No. 1900015.
- (15) Gao, S.; Hao, S.; Huang, Z.; Yuan, Y.; Han, S.; Lei, L.; Zhang, X.; Shahbazian-Yassar, R.; Lu, J. Synthesis of high-entropy alloy nanoparticles on supports by the fast moving bed pyrolysis. *Nat. Commun.* **2020**, 11, 2016.
- (16) Kusada, K.; Yamamoto, T.; Toriyama, T.; Matsumura, S.; Sato, K.; Nagaoka, K.; Terada, K.; Ikeda, Y.; Hirai, Y.; Kitagawa, H. Nonequilibrium Flow-Synthesis of Solid-Solution Alloy Nanoparticles: From Immiscible Binary to High-Entropy Alloys. *J. Phys. Chem. C* **2021**, 125, 458–463.
- (17) Minamihara, H.; Kusada, K.; Wu, D.; Yamamoto, T.; Toriyama, T.; Matsumura, S.; Kumara, L. S. R.; Ohara, K.; Sakata, O.;

- Kawaguchi, S.; Kubota, Y.; Kitagawa, H. Continuous-Flow Reactor Synthesis for Homogeneous 1 nm-Sized Extremely Small High-Entropy Alloy Nanoparticles. *J. Am. Chem. Soc.* **2022**, *144*, 11525–11529.
- (18) Konda, S. K.; Chen, A. Palladium based nanomaterials for enhanced hydrogen spillover and storage. *Mater. Today* **2016**, *19*, 100–108.
- (19) Collins, S. S. E.; Cittadini, M.; Pecharrómán, C.; Martucci, A.; Mulvaney, P. Hydrogen Spillover between Single Gold Nanorods and Metal Oxide Supports: A Surface Plasmon Spectroscopy Study. *ACS Nano* **2015**, *9*, 7846–7856.
- (20) Hülsey, M. J.; Fung, V.; Hou, X.; Wu, J.; Yan, N. Hydrogen Spillover and Its Relation to Hydrogenation: Observations on Structurally Defined Single-Atom Sites. *Angew. Chem., Int. Ed.* **2022**, *61*, No. e202208237.
- (21) Im, J.; Shin, H.; Jang, H.; Kim, H.; Choi, M. Maximizing the catalytic function of hydrogen spillover in platinum-encapsulated aluminosilicates with controlled nanostructures. *Nat. Commun.* **2014**, *5*, 3370.
- (22) Prins, R. Hydrogen Spillover Facts and Fiction. *Chem. Rev.* **2012**, *112*, 2714–2738.
- (23) Mori, K.; Miyawaki, K.; Yamashita, H. Ru and Ru–Ni Nanoparticles on TiO₂ Support as Extremely Active Catalysts for Hydrogen Production from Ammonia–Borane. *ACS Catal.* **2016**, *6*, 3128–3135.
- (24) Masuda, S.; Mori, K.; Sano, T.; Miyawaki, K.; Chiang, W. H.; Yamashita, H. Simple Route for the Synthesis of Highly Active Bimetallic Nanoparticle Catalysts with Immiscible Ru and Ni Combination by utilizing a TiO₂ Support. *ChemCatChem* **2018**, *10*, 3526–3531.
- (25) Masuda, S.; Shun, K.; Mori, K.; Kuwahara, Y.; Yamashita, H. Synthesis of a binary alloy nanoparticle catalyst with an immiscible combination of Rh and Cu assisted by hydrogen spillover on a TiO₂ support. *Chem. Sci.* **2020**, *22*, 4194–4203.
- (26) Mori, K.; Hashimoto, N.; Kamiuchi, N.; Yoshida, H.; Kobayashi, H.; Yamashita, H. Hydrogen spillover-driven synthesis of high-entropy alloy nanoparticles as a robust catalyst for CO₂ hydrogenation. *Nat. Commun.* **2021**, *12*, 3884.
- (27) Rodriguez, J. A.; Grinter, D. C.; Liu, Z.; Palomino, R. M.; Senanayake, S. D. Ceria-based model catalysts: fundamental studies on the importance of the metal–ceria interface in CO oxidation, the water–gas shift, CO₂ hydrogenation, and methane and alcohol reforming. *Chem. Soc. Rev.* **2017**, *46*, 1824–1841.
- (28) Machida, M.; Murata, Y.; Kishikawa, K.; Zhang, D.; Ikeue, K. On the Reasons for High Activity of CeO₂ Catalyst for Soot Oxidation. *Chem. Mater.* **2008**, *20*, 4489–4494.
- (29) Trovarelli, A.; Llorca, J. Ceria Catalysts at Nanoscale: How Do Crystal Shapes Shape Catalysis? *ACS Catal.* **2017**, *7*, 4716–4735.
- (30) Aneggi, E.; Wiater, D.; De Leitenburg, C.; Llorca, J.; Trovarelli, A. Shape-Dependent Activity of Ceria in Soot Combustion. *ACS Catal.* **2014**, *4*, 172–181.
- (31) Zhang, X.; You, R.; Li, D.; Cao, T.; Huang, W. Reaction Sensitivity of Ceria Morphology Effect on Ni/CeO₂ Catalysis in Propane Oxidation Reactions. *ACS Appl. Mater. Interfaces* **2017**, *9*, 35897–35907.
- (32) Hu, Z.; Liu, X.; Meng, D.; Guo, Y.; Guo, Y.; Lu, G. Effect of Ceria Crystal Plane on the Physicochemical and Catalytic Properties of Pd/Ceria for CO and Propane Oxidation. *ACS Catal.* **2016**, *6*, 2265–2279.
- (33) Sayle, D. C.; Maicaneanu, S. A.; Watson, G. W. Atomistic Models for CeO₂(111), (110), and (100) Nanoparticles, Supported on Yttrium-Stabilized Zirconia. *J. Am. Chem. Soc.* **2002**, *124*, 11429–11439.
- (34) Mori, K.; Jida, H.; Kuwahara, Y.; Yamashita, H. CoOx-decorated CeO₂ heterostructures: Effects of morphology on their catalytic properties in diesel soot combustion. *Nanoscale* **2020**, *12*, 1779–1789.
- (35) Guo, Y.; Mei, S.; Yuan, K.; Wang, D.-J.; Liu, H.-C.; Yan, C.-H.; Zhang, Y.-W. Low-Temperature CO₂ Methanation over CeO₂-Supported Ru Single Atoms, Nanoclusters, and Nanoparticles Competitively Tuned by Strong Metal–Support Interactions and H-Spillover Effect. *ACS Catal.* **2018**, *8*, 6203–6215.
- (36) Tournayan, L.; Marcilio, N. R.; Frety, R. Promotion of Hydrogen Uptake in Cerium Dioxide - the Role of Iridium. *Appl. Catal.* **1991**, *78*, 31–43.
- (37) Zhou, K.; Wang, X.; Sun, X.; Peng, Q.; Li, Y. Enhanced catalytic activity of ceria nanorods from well-defined reactive crystal planes. *J. Catal.* **2005**, *229*, 206–212.
- (38) Lu, X.; Zheng, D.; Zhang, P.; Liang, C.; Liu, P.; Tong, Y. Facile synthesis of free-standing CeO₂ nanorods for photoelectrochemical applications. *Chem. Commun.* **2010**, *46*, 7721.
- (39) Shun, K.; Mori, K.; Masuda, S.; Hashimoto, N.; Hinuma, Y.; Kobayashi, H.; Yamashita, H. Revealing hydrogen spillover pathways in reducible metal oxides. *Chem. Sci.* **2022**, *13*, 8137–8147.
- (40) Takeuchi, A.; Inoue, A. Classification of bulk metallic glasses by atomic size difference, heat of mixing and period of constituent elements and its application to characterization of the main alloying element. *Mater. Trans.* **2005**, *46*, 2817–2829.
- (41) Chen, J.; Yiu, Y. M.; Wang, Z.; Covelli, D.; Sammynaiken, R.; Finck, Y. Z.; Sham, T.-K. Elucidating the Many-Body Effect and Anomalous Pt and Ni Core Level Shifts in X-ray Photoelectron Spectroscopy of Pt–Ni Alloys. *J. Phys. Chem. C* **2020**, *124*, 2313–2318.
- (42) Bauer, J. C.; Mullins, D.; Li, M.; Wu, Z.; Payzant, E. A.; Overbury, S. H.; Dai, S. Synthesis of silica supported AuCu nanoparticle catalysts and the effects of pretreatment conditions for the CO oxidation reaction. *Phys. Chem. Chem. Phys.* **2011**, *13*, 2571.
- (43) Okamoto, K.; Akiyama, R.; Yoshida, H.; Yoshida, T.; Kobayashi, S. Formation of Nanoarchitectures Including Subnanometer Palladium Clusters and Their Use as Highly Active Catalysts. *J. Am. Chem. Soc.* **2005**, *127*, 2125–2135.
- (44) Nilsson, J.; Carlsson, P.-A.; Grönbeck, H.; Skoglundh, M. First Principles Calculations of Palladium Nanoparticle XANES Spectra. *Top. Catal.* **2017**, *60*, 283–288.
- (45) Lin, C.-M.; Hung, T.-L.; Huang, Y.-H.; Wu, K.-T.; Tang, M.-T.; Lee, C.-H.; Chen, C. T.; Chen, Y. Y. Size-dependent lattice structure of palladium studied by x-ray absorption spectroscopy. *Phys. Rev. B* **2007**, *75*, No. 125426.
- (46) Imaoka, T.; Kitazawa, H.; Chun, W.-J.; Omura, S.; Albrecht, K.; Yamamoto, K. Magic Number Pt₁₃ and Misshapen Pt₁₂ Clusters: Which One is the Better Catalyst? *J. Am. Chem. Soc.* **2013**, *135*, 13089–13095.
- (47) Herzog, A. A.; Kiely, C. J.; Carley, A. F.; Landon, P.; Hutchings, G. J. Identification of active gold nanoclusters on iron oxide supports for CO oxidation. *Science* **2008**, *321*, 1331–1335.
- (48) Brown, W. A.; King, D. A. NO Chemisorption and Reactions on Metal Surfaces: A New Perspective. *J. Phys. Chem. B* **2000**, *104*, 2578–2595.
- (49) Zhang, L.; Spezzati, G.; Muravev, V.; Verheijen, M. A.; Zijlstra, B.; Filot, I. A. W.; Su, Y.-Q.; Chang, M.-W.; Hensen, E. J. M. Improved Pd/CeO₂ Catalysts for Low-Temperature NO Reduction: Activation of CeO₂ Lattice Oxygen by Fe Doping. *ACS Catal.* **2021**, *11*, 5614–5627.
- (50) Jing, Y.; Cai, Z.; Liu, C.; Toyao, T.; Maeno, Z.; Asakura, H.; Hiwasa, S.; Nagaoka, S.; Kondoh, H.; Shimizu, K. I. Promotional Effect of Ia in the Three-Way Catalysis of La-Loaded Al₂O₃-Supported Pd Catalysts (Pd/La/Al₂O₃). *ACS Catal.* **2020**, *10*, 1010–1023.
- (51) Yasumura, S.; Ide, H.; Ueda, T.; Jing, Y.; Liu, C.; Kon, K.; Toyao, T.; Maeno, Z.; Shimizu, K.-I. Transformation of Bulk Pd to Pd Cations in Small-Pore CHA Zeolites Facilitated by NO. *JACS Au* **2021**, *1*, 201–211.
- (52) Mai, H. X.; Sun, L. D.; Zhang, Y. W.; Si, R.; Feng, W.; Zhang, H. P.; Liu, H. C.; Yan, C. H. Shape-selective synthesis and oxygen storage behavior of ceria nanopolyhedra, nanorods, and nanocubes. *J. Phys. Chem. B* **2005**, *109*, 24380–24385.
- (53) Wang, N.; Qian, W.; Chu, W.; Wei, F. Crystal-plane effect of nanoscale CeO₂ on the catalytic performance of Ni/CeO₂ catalysts for methane dry reforming. *Catal. Sci. Technol.* **2016**, *6*, 3594–3605.

- (54) Delley, B. An all-electron numerical method for solving the local density functional for polyatomic molecules. *J. Chem. Phys.* **1990**, *92*, 508–517.
- (55) Delley, B. From molecules to solids with the DMol3 approach. *J. Chem. Phys.* **2000**, *113*, 7756–7764.
- (56) Perdew, J. P.; Burke, K.; Ernzerhof, M. Generalized Gradient Approximation Made Simple. *Phys. Rev. Lett.* **1996**, *77*, 3865–3868.
- (57) Payne, M. C.; Teter, M. P.; Allan, D. C.; Arias, T. A.; Joannopoulos, J. D. Iterative minimization techniques for ab initio total-energy calculations: molecular dynamics and conjugate gradients. *Rev. Mod. Phys.* **1992**, *64*, 1045–1097.
- (58) Milman, V.; Winkler, B.; White, J. A.; Pickard, C. J.; Payne, M. C.; Akhmatkaya, E. V.; Nobes, R. H. Electronic structure, properties, and phase stability of inorganic crystals: A pseudopotential plane-wave study. *Int. J. Quantum Chem.* **2000**, *77*, 895–910.
- (59) Mizoguchi, T.; Tanaka, I.; Gao, S.-P.; Pickard, C. J. First-principles calculation of spectral features, chemical shift and absolute threshold of ELNES and XANES using a plane wave pseudopotential method. *J. Phys.: Condens. Matter* **2009**, *21*, No. 104204.